International Journal of Heat and Mass Transfer 80 (2015) 458–468

Contents lists available at ScienceDirect

International Journal of Heat and Mass Transfer

journal homepage: www.elsevier.com/locate/ijhmt

An X-type lattice cored ventilated brake disc with enhanced cooling performance

H.B. Yan [a], Q.C. Zhang [b], T.J. Lu [b,*]

[a] School of Energy and Power Engineering, Xi'an Jiaotong University, Xi'an 710049, China
[b] State Key Laboratory for Mechanical Structure Strength and Vibration, Xi'an Jiaotong University, Xi'an 710049, China

ARTICLE INFO

Article history:
Received 16 May 2014
Received in revised form 11 September 2014
Accepted 24 September 2014
Available online 11 October 2014

Keywords:
Ventilated brake disc
X-type lattice
Radial vane
Heat transfer enhancement
Anisotropy

ABSTRACT

To improve the cooling performance of a disc brake system, we introduce a new concept of bidirectional ventilated brake disc with an X-type lattice core. Transient and steady-state thermo-fluidic behaviors of the new brake disc are experimentally characterized and compared with a prevalent radial vane brake disc under identical conditions. Transient heating-up tests at a constant rotating speed, simulating continuous downhill braking, show that both brake discs exhibit a similar temperature during initial period, whilst evidently lower temperature can be achieved by the new brake disc under steady-state conditions. For a given rotating speed in typical operating range (i.e., 200–1000 rpm), steady-state tests reveal that the new brake disc provides 1–14% higher overall Nusselt number than the reference one. Although the X-type lattice core provides 43% less pumping capacity than radial vanes, more complex flow mixing and 1.1 times more heat transfer area caused by the lattice core are responsible for the superior overall cooling performance of the new brake disc. In addition, the morphological anisotropy of the lattice core induces circumferentially non-uniform heat transfer in the disc. The most open orientation of the lattice core provides substantially higher heat transfer than the most blocked orientation. Mechanisms of the anisotropic heat transfer pattern are experimentally explored.

1. Introduction

Hydraulically actuated disc brakes are widely used in passenger vehicles for their superior cooling performance relative to drum brakes [1,2]. As shown schematically in Fig. 1(a), to decelerate a vehicle, the friction between the brake disc and pads transforms kinetic and potential energies into thermal energy. During high-load braking such as repeated high-speed braking and continuous downhill braking, frictional heating can substantially raise temperature at the friction interface (e.g., up to 900 K) [3–5], leading ultimately to overheating of braking components such as brake discs and pads. A multitude of studies have reported that such overheating can cause brake fade (i.e., deterioration of friction coefficient) [6–9], increased wear of the friction pair [10] and thermal cracking of the brake disc [5,11,12]. Therefore, sufficient cooling of braking components is crucial to braking performance and safety, especially for high performance passenger vehicles.

To prevent brake fluid boiling in the caliper cylinder, heat accumulation in brake pads needs to be minimized [9]. Consequently, a majority of the frictional heat (approximately 90% [13]) is transferred to the brake disc. To effectively remove the transferred heat, brake discs are often designed to have an additional ventilated channel configured by two rubbing discs that sandwich various heat dissipation elements; see Fig. 1(c)–(e). These centrifugal fan-like ventilated brake discs draw ambient air into the ventilated channel when the brake disc rotates [14]. Compared to a solid brake disc (see Fig. 1(b)), substantially improved cooling can be achieved due to forced convection through the core elements [15]. Since the popular application of disc brakes in passenger vehicles in the 1960s [1], considerable efforts have been devoted to developing thermally more effective brake discs by optimizing the heat dissipation elements arranged in the ventilated channel. Thereupon, three different types of ventilated brake discs consisting of pin–fins, radial vanes and curved vanes have been devised as illustrated in Fig. 1(c)–(e) [16].

Amongst these ventilated brake discs, a pin-finned brake disc (see Fig. 1(c)) provides the worst overall cooling performance due mainly to its poor pumping capacity [17,18], whereas more uniform temperature distribution exists in its rubbing discs [19]. This type of ventilated brake disc is mainly used in heavy-duty trucks to prevent catastrophic thermal cracking of the disc induced

* Corresponding author. Tel.: +86 029 82665937.
E-mail addresses: hongbinyanhb@163.com (H.B. Yan), zqc111999@mail.xjtu.edu.cn (Q.C. Zhang), tjlu@mail.xjtu.edu.cn (T.J. Lu).

http://dx.doi.org/10.1016/j.ijheatmasstransfer.2014.09.060
0017-9310/

Nomenclature

b_1, b_2	widths of the intersection point in Fig. 4(c) (m)
c_p	specific heat of fluid (J/(kg K))
f_H	friction factor defined in Eq. (7)
h	heat transfer coefficient (W/(m^2 K))
H	height of a ventilated channel (m)
H_{h1}, H_{h2}	axial dimensions of a brake hub (m)
k	thermal conductivity of fluid (W/(m K))
l	length of an X-type lattice core unit cell (m)
L_{v1}, L_{v2}	lengths of long and short radial vanes (m)
$\dot{m}$	mass flow rate (kg/s)
N	rotating speed of a brake disc (rpm)
Nu_H	area-averaged Nusselt number defined in Eq. (8)
Nu_{Ro}	local Nusselt number defined in Eq. (4)
$Nu_{Ro,\ m}$	area-averaged Nusselt number for brake discs
q''	heat flux (W/m^2)
Q	total power input (W)
r	radial coordinate (m)
r_1-r_3	fillet radii shown in Fig. 4(d) and (e) (m)
R_{duct}	inner radius of a circular intake duct (m)
Re_H	Reynolds number defined in Eq. (6)
Re_{Ro}	rotational Reynolds number defined in Eq. (3)
R_{h1}, R_{h2}	radial dimensions of a brake hub (m)
R_i, R_o	inner and outer radii of a rubbing disc (m)
R_v	radial location of radial vanes (m)
t	time (s)
t_l	thickness of an X-type lattice core ligament (m)
t_r	thickness of a rubbing disc (m)
t_v	thickness of radial vanes (m)
T_a	ambient air temperature (K)
T_f	bulk mean fluid temperature in Eq. (10) (K)
T_{in}	inlet fluid temperature (K)
T_w	local wall temperature (K)
$T_{w,\ m}$	area-averaged wall temperature (K)
U	axial velocity component in a circular intake duct (m/s)
U_c	centerline velocity in a circular intake duct (m/s)
U_m	mean velocity in a rectangular channel (m/s)
w	width of X-type lattice core unit cell (m)
w_l	width of X-type lattice core ligament (m)
z	axial coordinate depicted in Fig. 3(a) (m)
z'	Cartesian coordinate component in Fig. 7 (m)

Greek symbols

α, β	included angles shown in Fig. 4(d, e) (°)
Δp	pressure drop (Pa)
ε_v	porosity of a radial vane core
ε_X	porosity of an X-type lattice core
θ	azimuth coordinate (°)
μ	dynamic viscosity of fluid (Pa s)
ρ	density of fluid (kg/m^3)
$\rho_{SA,\ X}$	surface area density of an X-type lattice core (m^2/m^3)
$\rho_{SA,\ v}$	surface area density of a radial vane core (m^2/m^3)
ω	angular velocity (rad/s)

Abbreviations

OA	orientation A
OB	orientation B
rpm	revolution per minute

by severe braking load, while its application in passenger vehicles is limited. Flow and temperature fields at the cooling channel exit of such a brake disc have been measured and numerically simulated by Barigozzi et al. [20,21]. Optimization has been conducted by Palmer et al. [22,23] to improve the cooling performance by changing the cross-section and arrangement of pin–fins.

Brake discs with vane-type cores of Fig. 1(d) and (e) have been widely used in passenger vehicles. According to the dependence of aerodynamic and thermal performances upon rotating direction, these brake discs are classified into bidirectional and unidirectional brake discs. The radial vane brake disc (see Fig. 1(d)) is a typical bidirectional brake disc which ensures identical cooling performance when mounted to the left and right wheels of a passenger vehicle. Consequently, this type of brake disc is the most popular choice [16]. Numerous studies have been conducted to characterize its thermo-fluidic characteristics [3,14,24–31] and to improve its cooling performance by modifying the cross-section and arrangement of radial vanes [17–19,32–36]. It is demonstrated that cooling flow turns to the counter-rotating direction with respect to the brake disc axis before entering the ventilated channel. Due to the Coriolis effect, the incident flow angle to the vane is large, causing flow separation from the leading edge of the vane. Consequently, a large flow recirculation region forms nearby the suction side of each vane, reducing the amount of cooling flow drawn into the ventilated channel and hence deteriorating the cooling performance. This is a common and intrinsic problem associated with such brake discs.

Curved vanes of Fig. 1(e) are designed to increase the mass flow rate of cooling flow into the ventilated channel by minimized flow blockage as a result of suppressed flow separation. Consequently, cooling performance is further improved [37–39]. However, this type of brake disc is unidirectional, requiring a mirrored pair for two sides of the wheels. The consequent inconvenience for maintenance has restricted its widespread application, and only limited investigations are available in the open literature [37–40].

Although the cooling performance of the brake discs described above can be improved, constraints by the casting method make it difficult to optimize every aspect of the design. Pin–fins and vanes in current ventilated brake discs are prismatic and thick, configured two-dimensionally normal to the rubbing discs. This configuration may not be favorable for forced convective heat transfer due to limited flow mixing and heat transfer area. Such a situation motivates the authors to introduce recently developed novel heat dissipation elements into a ventilated brake disc to further improve its cooling performance.

During the selection and design of heat dissipation elements for brake discs, a special service environment has to be considered. During braking, continuous clamping force is applied upon rotating rubbing discs by brake pads, causing both compression and shear on core elements. According to an internationally well recognized regulation for vehicle braking systems, ECE R13-H, the compressive and shear stresses exerted by the brake pads are estimated to be up to 3 MPa and 1.2 MPa for a typical passenger vehicle with a weight of 1.5 tons, respectively. Therefore, in addition to heat removal capability, the core elements distributed in the ventilated channel must be sufficiently stiff and strong. To this end, a variety of multi-functional periodic cellular materials (PCMs) [41] (see Fig. 2) with fluid-through cellular three-dimensional topologies and thin solid ligaments appear to be promising heat dissipation media for the ventilated brake disc. Such PCMs provide excellent capability of bearing simultaneous mechanical and thermal loads [41–44], which meets the mechanical requirements especially compressive and shear strengths for ventilated brake disc.

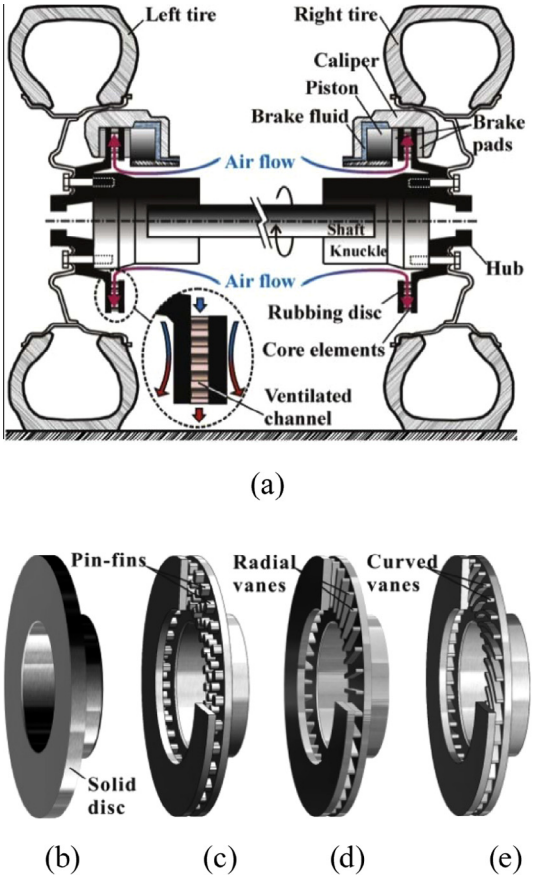

Fig. 1. Schematic illustration of a passenger vehicle disc brake system: (a) components and working principle; (b) solid brake disc; (c)–(e) ventilated brake discs with pin–fins, radial vanes and curved vanes.

The development of PCMs has been promoted by recent advances in manufacturing technologies. Thus far, several fabrication methods have been introduced including metal wire weaving [45], investment casting [46], cylinder assembling [47], and metal sheet folding [48]. In particular, metal sheet folding is considered simple and more cost effective [41]. With this method, PCMs having different cell topologies (e.g., tetrahedron and pyramid) can be implemented [41]. However, the fabrication of a tetrahedral lattice inevitably requires the perforation of a complete metal sheet to form hexagonal holes [48], thus wasting a considerable amount of material. For a pyramidal lattice (see Fig. 2(c)), however, an alternative method of slitting and expanding a complete metal sheet has been developed to form the required diamond holes, allowing close to 100% material to be utilized [49].

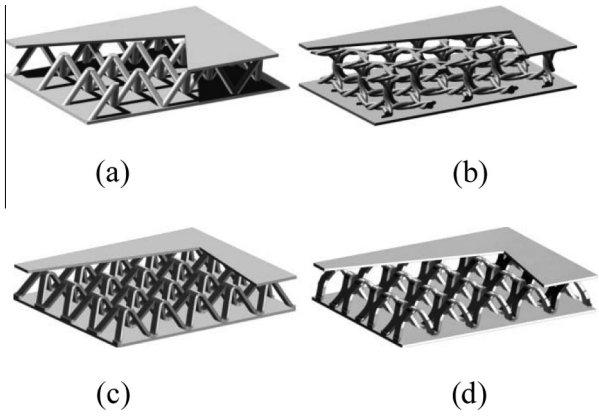

Fig. 2. Schematics of lightweight sandwich panels with (a) tetrahedral, (b) Kagome, (c) pyramidal and (d) X-type lattice cores for simultaneous mechanical and thermal loads bearing applications.

Similar to the pyramidal lattice, a new lattice with ligaments intersecting into an X shape, the so-called X-type lattice (see Fig. 2(d)), has been developed. These two lattices can be fabricated by folding an identical metal sheet with the same set of moulds. However, the X-type lattice is mechanically superior, providing approximately 30% higher peak compressive and shear strengths for a given relative density (or porosity) [50,51].

This study, therefore, introduces a new concept of bidirectional ventilated brake disc that is thermally more effective for passenger vehicles. A high porosity yet mechanically strong X-type lattice is incorporated into the brake disc as core. Its transient and steady-state thermo-fluidic behaviors are experimentally characterized and compared to a prevalent bidirectional radial vane brake disc.

2. Experimental details

2.1. Test details in a rotating environment

During actual braking, fluid flow around a ventilated brake disc is fairly complicated due to the influences of suspension system, wheel assembly and incoming flow induced by the movement of a vehicle. As a result, investigations in an in-situ environment are difficult and costly. Consequently, the present study focuses on a brake disc rotating in an infinite environment, without considering the aforementioned additional influences. Such a scheme has been adopted in most previous studies and is believed to be reasonable at the preliminary design stage for comparative investigations [4,5,13–15,17–26,29,31,33–40].

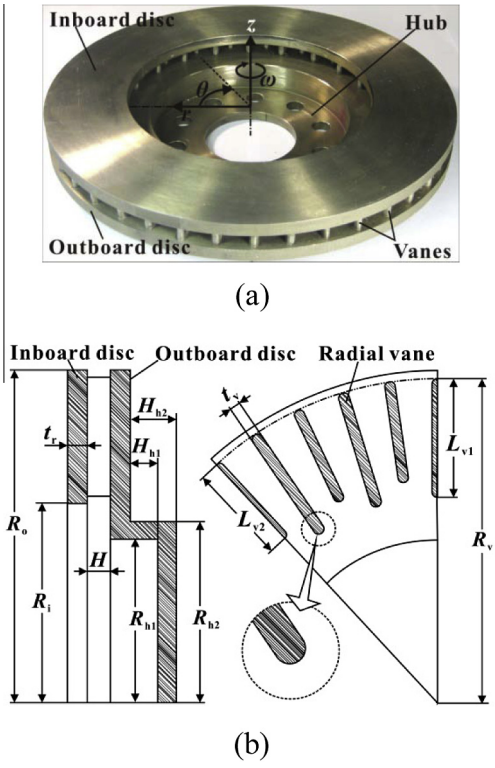

Fig. 3. Details of a commercially available radial vane brake disc: (a) as-fabricated sample; (b) geometric details.

2.1.1. Tested brake disc samples

First, for reference, a bidirectional radial vane brake disc which is prevalent for passenger vehicles [16] is tested. This sample incorporates a total of 42 alternatively arranged short and long radial vanes protruding from the inboard and outboard discs (see Fig. 3). These vanes have identical thickness (t_v), with fillets at both ends.

The casting process endows the reference brake disc with large uncertainties in its geometric dimensions, which is not suitable for a systematic comparison. Therefore, the brake disc is duplicated using AISI 304 stainless steel with a thermal conductivity of 16.2 W/(m K) [52]. Vanes are first fabricated by wire-electrode cutting and then brazed to two rubbing discs with identical thickness (t_r). The brazing procedures are the same as those described in [50]. Detailed geometric parameters of this test sample are illustrated in Fig. 3(b) and summarized in Table 1. The porosity (ε_v) and surface area density ($\rho_{SA,\,v}$) of the radial vane core are calculated to be 0.773 and 98 m^2/m^3, using the following formulae:

$$\varepsilon_v = 1 - \frac{21\left[(L_{v1}+L_{v2})t_v + (\pi/2-2)t_v^2\right]}{\pi\left(R_o^2 - R_i^2\right)} \quad (1)$$

$$\rho_{SA,\,v} = \frac{42[(L_{v1}+L_{v2}) + (\pi-2)t_v]}{\pi\left(R_o^2 - R_i^2\right)} \quad (2)$$

An X-type lattice cored brake disc is also fabricated from AISI 304 stainless steel for consistency. A single layer of X-type lattice is first fabricated by folding a perforated metal sheet with staggered diamond holes. The material block is subsequently cut into an annular shape; see Fig. 4(a). Afterwards, the core is brazed onto two metallic discs in a vacuum furnace to form the complete brake disc; see Fig. 4(b). Fabrication details for the X-type lattice and brazing procedures are documented in [50].

The annular X-type lattice core has identical inner and outer radii with inboard disc. A unit cell of the X-type lattice and the corresponding front views in two mutually perpendicular orientations are shown in Fig. 4(c)–(e). The morphology of the unit cell depends on nine independent dimensions, i.e., l, w, H, w_1, t_l, r_1, r_2, α and β. Other parameters, i.e., b_1, b_2, r_3, porosity (ε_X) and surface area density ($\rho_{SA,\,X}$), can subsequently be calculated from the formulae given in [53]. Detailed geometric parameters of the present X-type lattice core are summarized in Table 2. Other dimensions of the X-type lattice cored brake disc are identical to those of the radial vane brake disc.

As previously mentioned, the heat dissipation elements must be able to sustain the clamping force applied by the brake pads. Consequently, quasi-static compression test is conducted on the present lattice core following the same procedures as those in [50]. Its equivalent compressive strength is measured to be 9.13 MPa. Therefore, according to ECE R13-H, this lattice core is mechanically strong enough for applications in standard passenger vehicles. For brevity, details of the compression test and clamping force estimation are not shown here.

Table 1
Geometric parameters of radial vane brake disc.

Parameter	Value (m)	Parameter	Value
H	0.00966	R_i	0.09 m
H_{h1}	0.013	R_o	0.15 m
H_{h2}	0.021	R_v	0.147 m
L_{v1}	0.054	t_r	0.009 m
L_{v2}	0.046	t_v	0.005 m
R_{h1}	0.074	ε_v	0.773
R_{h2}	0.082	$\rho_{SA,\,v}$	98 m^2/m^3

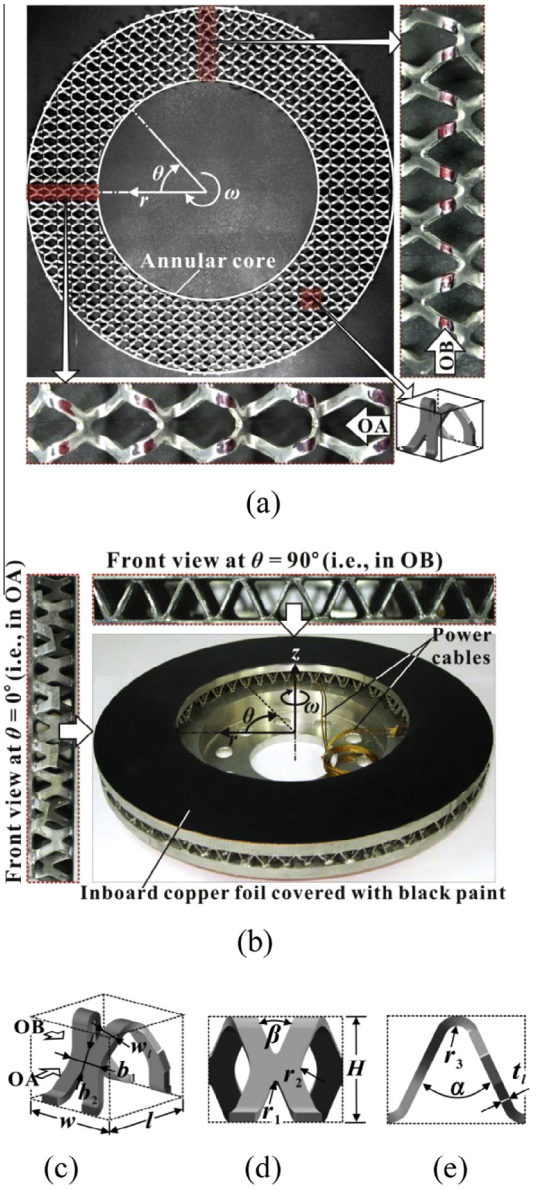

Fig. 4. Details of X-type lattice cored brake disc: (a) as-fabricated annular X-type lattice; (b) as-fabricated brake disc; (c) unit cell of the X-type lattice; (d) front view of unit cell in orientation A (OA); (e) front view of unit cell in orientation B (OB).

Table 2
Morphological parameters of X-type lattice.

Parameter	Value (m)	Parameter	Value
b_1	0.00462	w	0.012 m
b_2	0.0027	w_l	0.00216 m
l	0.012	α	50°
r_1	0.0003	β	42°
r_2	0.0043	ε_X	0.932
r_3	0.00105	$\rho_{SA,\,X}$	205 m^2/m^3
t_l	0.00091		

2.1.2. Rotating test rig

A rotating test rig is designed and constructed to characterize the thermo-fluidic behaviors of a brake disc; see Fig. 5(a). A portable base frame equipped with wheels is first fabricated, which is then propped up by rubber supports to minimize mechanical vibration during experiments. A 3-phase AC motor mounted on the base frame is connected to a shaft through a flexible coupling. The shaft is supported by two deep groove ball bearings. The brake

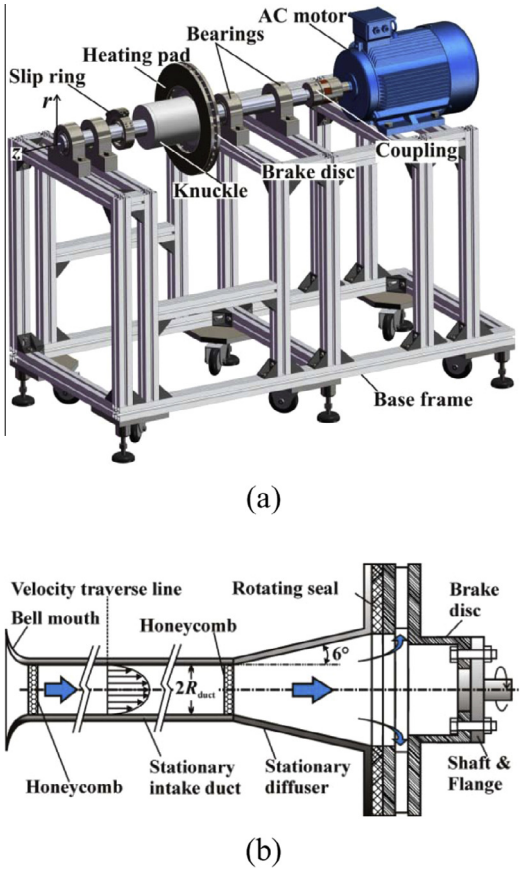

Fig. 5. Test facilities for brake discs: (a) rotating test rig; (b) test section for pumping capacity measurement.

disc is fixed to the shaft through a flange. Another removable shaft supported by two additional bearings is bolted to the former one to allow an acrylic component modeling the knuckle (outer diameter 0.12 m) and a four-channel slip ring to be mounted. Electrical noise of the slip ring (from Pan-Link Electrical technology Co., Ltd., China) is less than 0.04 Ω, which is negligible compared to the electrical resistance of each heating element (i.e., 41 Ω). Rotating speed of the brake disc is controlled by an inverter connected to the AC motor and measured by a digital tachometer (from Lutron Electronic Enterprise Co., Ltd., Taiwan) with a resolution of 0.1 rpm.

2.1.3. Heat transfer measurement

During actual braking, heat is generated by sliding friction between the brake disc and pads. A majority of the heat is transferred to the brake disc and ultimately removed from the surfaces of rubbing discs and heat dissipation elements. Actual heat flux distribution on the friction interface is highly complicated, depending on various factors such as wear conditions of the friction pair. Since comparative overall cooling performance of the two brake discs is of concern in the current study, a constant and identical heat flux of 3640 W/m^2, corresponding to a total power input (Q) of 329 W, is imposed by two annular film heating elements attached to both inboard and outboard discs via thermally conductive double sided tape. The slip ring connects these heating elements to a DC power supply (Agilent™ 6655A). Copper foils having thickness of 6×10^{-5} m are then attached to the heating elements to remedy the non-uniformity of heat flux induced by gaps between the etched heating wires.

An infrared camera (Fluke™ Ti50) with a resolution of 320×240 pixels is used to measure temperature field on the surface of inboard copper foil that is covered by black paint to offer an emissivity of approximately 1.0; see Fig. 4(b). Before testing, the infrared camera is calibrated when the brake disc is stationary. This is realized by comparing the temperature readings at the same point measured by the infrared camera and a foil type thermocouple (Omega™, thickness 1×10^{-4} m) attached to the black paint layer. In addition, a bead type thermocouple (Omega™) is used to measure the ambient air temperature as reference. Detailed operating conditions are summarized in Table 3.

2.1.4. Pumping capacity measurement

To facilitate the measurement of pumping capacity for each brake disc, a separate test section is constructed as illustrated in Fig. 5(b). The knuckle, the slip ring and the corresponding supporting shaft and bearings are firstly removed from the test rig in Fig. 5(a). Instead, a small angle diffuser (with a divergence angle of 12°) made of aluminum is supported by a purpose built fixing frame and is connected to the inlet of the ventilated brake disc. To minimize possible flow leakage, a closed-cell foam type seal is tightly sandwiched between the brake disc and diffuser during installation of the test section. Subsequently, a circular intake duct (R_{duct} = 0.05 m) with a length of 0.65 m is connected to the inlet of the diffuser, in which two honeycomb layers are inserted immediately at the inlet and outlet of the flow tube; see Fig. 5(b). The aluminum honeycomb (thickness 0.015 m) has hexagonal holes with an edge length of 3×10^{-3} m and a wall thickness of 5×10^{-5} m. During measurements, the diffuser and intake duct remain stationary contrast to the rotating brake disc.

Once the brake disc starts to rotate, air at ambient conditions is continuously sucked in through a bell mouth which is used to eliminate severe flow separation. The axial velocity component (along the z-axis) is then traversed along the radial direction (i.e., the r-axis) by a Pitot tube (outer diameter 3×10^{-3} m) in the circular intake duct. The velocity traverse line is located at mid-length of the intake duct. Pumping capacity is obtained by integrating the measured velocity profile.

2.2. Test details in a stationary wind tunnel

Test results reveal that local heat transfer on the inboard copper foil surface of the X-type lattice cored brake disc is circumferentially anisotropic. To explore the underlying mechanisms, forced convective pressure drop and heat transfer in sandwich panels representing typical orientations of the X-type lattice are measured in a stationary wind tunnel.

2.2.1. Tested sandwich panels

With reference to Fig. 6, two rectangular X-type lattice cores representing two typical orientations, i.e., OA and OB shown in Fig. 4, are brazed onto AISI 304 stainless steel substrates (thickness 9×10^{-4} m). They represent the most blocked and open orientations of the X-type lattice, respectively. Both samples contain eleven unit cells in the transverse direction to minimize sidewall effects and five unit cells in the streamwise direction for consistency with the annular core of Fig. 4(a). The morphological parameters of the rectangular lattice cores are identical to those of the annular core.

2.2.2. Test facilities

The test rig consists of an air supply system, a test section and a data acquisition system. With reference to Fig. 7, an open-circuit blow-down wind tunnel supplies air into a test section accommodating the test sample. The test channel is made of low-conducting acrylic plates. In front of the test sample, a honeycomb straighter is installed followed by a long parallel passage (length 48H) to make incoming flow fully developed. The X-type lattice sandwich panel

Table 3
Operating conditions of heat transfer measurements.

Tested sample	Parameter	Value
Brake discs	Rotational speed, N	200–1000 rpm
	Ambient air temperature, T_a	283.5–285.6 K
	Total power input, Q	329 W
Sandwich panels	Mean velocity, U_m	1.8–12.0 m/s
	Inlet air temperature, T_{in}	293.3–297.4 K
	Heat flux, q''	3200–9800 W/m^2

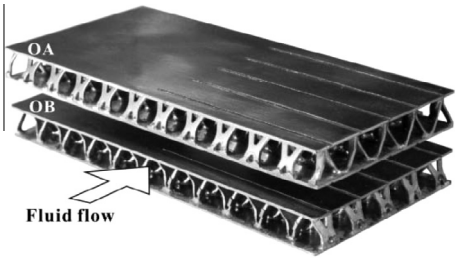

Fig. 6. As-fabricated X-type lattice sandwich panels.

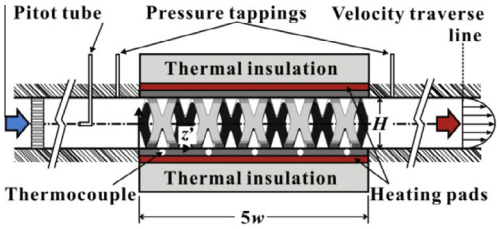

Fig. 7. Schematic of the test section connected to a stationary wind tunnel for pressure drop and heat transfer measurements.

is inserted into the channel with the inner surfaces of its substrates flush with channel inner surfaces.

2.2.3. Velocity and pressure drop measurements

To quantify the mass flow rate of convective flow through the X-type lattice core, the velocity profile at the exit of a long parallel flow channel (50H in length) placed downstream the test sample is traversed along channel height; see Fig. 7. To this end, a stagnation pressure probe (diameter 4×10^{-4} m) is installed on a linear traverse table (from Velmex Inc.) in conjunction with a static pressure tapping drilled through the upper channel wall. The mean velocity over channel height (U_m) is obtained by integrating the measured velocity profile and, for convenience, correlated as a function of the measured inlet centerline velocity measured by a separate Pitot tube placed upstream the test sample [53]. The mean velocity is set to vary from 1.8 m/s to 12.0 m/s during measurements, covering typical mean velocity range at the ventilated channel inlet of a brake disc during actual braking [26–28].

Two static pressure tappings are installed on the upper endwall (6×10^{-3} m upstream and downstream the test sample, respectively) to measure pressure drop during heat transfer measurement.

2.2.4. Heat transfer measurement

Identical and constant heat flux is imposed on both substrates of each sandwich panel by film heating elements connected to a DC power supply (Agilent™ 6655A). Five T-type bead thermocouples (Omega™) are arranged in the bottom substrate along the z'-axis to measure the endwall temperature; see Fig. 7. These thermocouples (4×10^{-4} m in diameter) are embedded in grooves (5×10^{-4} m in depth) machined on the outer surface of the bottom substrate. Each thermocouple is located at the center of the substrate corresponding to each unit cell. A thermal adhesive (Arctic Silver™) is used to fill the gap between the heating elements and the substrates. The test section is covered by thick thermally low-conducting foam to minimize heat loss.

Two additional T-type bead thermocouples are installed upstream and downstream the test sample to measure inlet and outlet coolant temperatures. All the measurements are conducted under steady-state conditions. Detailed operating conditions are summarized in Table 3.

2.3. Data reduction

For rotating tests, the rotational Reynolds number (Re_{Ro}) and local effective Nusselt number (Nu_{Ro}) based on the outer radius of the rubbing disc (R_o) are employed, defined as:

$$Re_{Ro} = \frac{\rho \omega R_o^2}{\mu} \tag{3}$$

$$Nu_{Ro}(r,\theta) = \frac{h(r,\theta) R_o}{k} \tag{4}$$

where ρ, μ and k denote the density, dynamic viscosity and thermal conductivity of air, respectively; and ω is the angular velocity of the rotating brake disc. $h(r,\theta)$ represents the local effective heat transfer coefficient, defined as:

$$h(r,\theta) = \frac{Q \Big/ \left[2\pi\left(R_o^2 - R_i^2\right)\right]}{T_w(r,\theta) - T_a} \tag{5}$$

where Q is the total power input by the two heating elements; $T_w(r,\theta)$ is local wall temperature on inboard copper foil surface measured by the infrared camera; and T_a is ambient air temperature. It should be mentioned that the inputted heat is first transferred to both sides of each heating element and then dissipated by both external (outside the ventilated channel) and internal (inside the ventilated channel) convective flows; see Fig. 1(a). Therefore, the effective heat transfer coefficient introduced in this study is a comprehensive evaluation of contributions by these two heat transfer mechanisms.

For forced convection in the wind tunnel, the Reynolds number (Re_H) and friction factor (f_H) based on channel height (H) are defined as:

$$Re_H = \frac{\rho U_m H}{\mu} \tag{6}$$

$$f_H = \frac{\Delta p}{5w} \frac{H}{\rho U_m^2/2} \tag{7}$$

where Δp is the pressure drop measured by inlet and outlet pressure tappings. For heat transfer evaluation, the area-averaged Nusselt number is used defined as:

$$Nu_H = \frac{1}{5}\sum_1^5 \left[\frac{h(z')H}{k}\right] \tag{8}$$

The local heat transfer coefficient, i.e., $h(z')$ in Eq. (8), is defined as:

$$h(z') = \frac{q''}{T_w(z') - T_f(z')} \tag{9}$$

where $T_w(z')$ is substrate inner surface temperature measured by thermocouples, with temperature drop through the substrate subtracted by one-dimensional heat conduction. $T_f(z')$ represents local bulk mean air temperature calculated from the energy balance of air as:

$$T_f(z') = T_{in} + \frac{2z'q''}{\rho U_m H c_p} \quad (10)$$

where T_{in} is inlet air temperature; q'' is heat flux imposed on each substrate by the heating element; and c_p is specific heat of air.

2.4. Measurement uncertainties

An uncertainty analysis is performed using the root mean square method [54]. For rotating test results, the thermo-physical properties of air based on ambient pressure and temperature are used in data reduction, with their uncertainties neglected. The uncertainty of rotating speed is found to be less than 4 rpm, resulting in an uncertainty of less than 4.0% for the rotational Reynolds number (Re_{Ro}). Pressure is measured by a differential pressure transducer (DSA 3217, Scanivalve™) with a resolution of 0.3 Pa. Consequently, the uncertainty associated with the cooling flow rate ($\dot{m}$) sucked into the ventilated channel is estimated to be less than 6.1%. Ambient air temperature (T_a) is measured by a T-type thermocouple (Omega™) with a resolution of 0.1 K. For each test, the fluctuation of ambient temperature is measured to be less than 0.5 K. The temperature measured by the infrared camera shows a maximum deviation of 0.2 K from that measured by the foil type thermocouple used for calibration. Therefore, the uncertainty associated with wall temperature is estimated to be less than 0.3 K. Consequently, the uncertainties for the effective heat transfer coefficient and Nusselt number (Nu_{Ro}) are estimated to be less than 3.0%.

For test results obtained in the wind tunnel, the density and dynamic viscosity of air are derived based on inlet static pressure and temperature, and hence their uncertainties are neglected. Pressure is also measured by the aforementioned pressure transducer. Consequently, the uncertainties associated with the Reynolds number (Re_H) and friction factor (f_H) are estimated to be less than 5.7% and 8.7%, respectively. Heat loss through channel walls is estimated by performing energy balance based on heat input and measured inlet and outlet air temperatures; and is found to be less than 4.5%. Temperatures from T-type thermocouples (Omega™) with an uncertainty of 0.1 K are recorded by an Agilent 34970A data logger. The thermal conductivity of air is evaluated at the arithmetic mean value of the inlet and outlet air temperatures. Its uncertainty is estimated to be less than 2.4% (within the operating range of 295–314 K). Consequently, the uncertainties for the heat transfer coefficient and Nusselt number (Nu_H) are estimated to be less than 6.4% and 6.8%, respectively.

3. Discussion of results

3.1. Transient and steady-state cooling performance

The braking system of a passenger vehicle experiences a variety of braking modes such as short-time stop braking and long-time downhill braking. Heat transfer associated with the ventilated brake disc can therefore be either transient or steady-state. To facilitate a comprehensive comparison of brake discs undergoing these distinct heat transfer processes, long-time downhill braking at constant vehicle speed of 100 km/h is experimentally simulated. To this end, the heating elements are switched on after the brake disc is accelerated to a rotating speed (N) of 800 rpm. The temperature field on the inboard copper foil surface is then continuously measured by the infrared camera.

Fig. 8(a) presents representative temperature fields measured at time t = 3600 s during transient tests for both types of brake disc. The results demonstrate clearly that the X-type lattice cored brake disc has lower surface temperature than the radial vane brake disc. Due to blockage by the base frame and bearings of the test rig (see Fig. 5(a)), only the upper half temperature field covering the azimuth angle of 0–180° is measured. The lower half is a central symmetry of the upper half due to identical structural periodic angle (180°) for both brake discs. In addition, the temperature at each point is actually the azimuthally averaged value as a result of the low frame rate of the infrared camera.

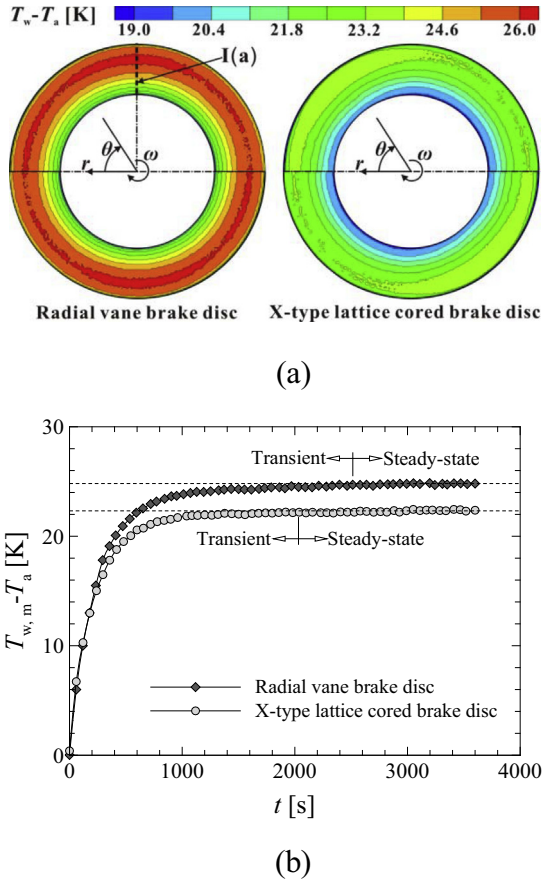

Fig. 8. Comparison of transient thermal behaviors of two different brake discs at N = 800 rpm: (a) representative temperature distribution on inboard copper foil surface at t = 3600 s; (b) evolution of area-averaged surface temperature.

To clarify the transient thermal response of each brake disc, the area-averaged surface temperature ($T_{w,m}$) obtained from a series of temperature fields including those in Fig. 8(a) is plotted in Fig. 8(b) as a function of time (t). For a given brake disc, its thermal capacity and effective heat transfer coefficient govern its transient thermal behavior. During the initial period (e.g., t < 200 s), heat dissipation is limited due to low temperature difference between the brake disc surface and cooling flow. Instead, a majority of thermal energy is absorbed by the brake disc. Therefore, the thermal capacity dominates the initial rise of surface temperature. Although the X-type lattice core is 70% lighter than the radial vane core, the total weight of the new brake disc is only 6% lower than that of the radial vane brake disc. Their similar thermal capacities result in comparable surface temperatures. With further increase of surface temperature, heat dissipation becomes increasingly more prominent, highlighting the dominance of effective heat transfer coefficient on surface temperature. Consequently, the superiority of the new brake disc becomes more evident as the transient process approaches steady-state. Once the heat transfer reaches steady-state, the surface temperature becomes constant, governed now completely by the effective heat transfer coefficient. At this point, the superiority of the X-type lattice cored brake disc is maximized, corresponding to approximately 10% reduction in surface

temperature as shown in Fig. 8(b). It can be concluded that during short-time braking, e.g., emergency stop braking, both brake discs operate at a similar temperature. However, during long-time braking such as repeated braking on the urban road and long-time downhill braking, the new brake disc exhibits a lower operating temperature.

In addition to braking mode, the operating temperature of a ventilated brake disc is also dependent upon rotating speed (i.e., vehicle speed) [31]. Therefore, the steady-state thermal behavior of each brake disc is characterized for a wide range of rotating speed from 200 rpm to 1000 rpm. The distribution of effective Nusselt number is firstly obtained according to Eq. (4) from each temperature field such as those presented in Fig. 8(a). The area-averaged effective Nusselt number ($Nu_{Ro,\ m}$) calculated thence using a customized computer program is plotted in Fig. 9. The Nusselt number can be correlated as a function of rotational Reynolds number as:

$$Nu_{Ro,m} = CRe_{Ro}^{n} \tag{11}$$

where $C = 0.9725$ and $n = 0.5806$ for the radial vane brake disc; $C = 0.4619$ and $n = 0.6526$ for the X-type lattice cored brake disc. The results of Fig. 9 demonstrate that, for both brake discs, the Nusselt number increases monotonically as the rotational Reynolds number is increased. The X-type lattice cored brake disc exhibits 1% (at 200 rpm) to 14% (at 1000 rpm) higher heat removal capacity than the radial vane brake disc, showing more pronounced superiority at higher vehicle speed.

3.2. Local heat transfer characteristics

Although the new brake disc provides better overall or area-averaged cooling performance than the reference brake disc, the highly anisotropic morphology of the X-type lattice core may cause anisotropic local heat transfer distribution. Revealing such characteristics is beneficial for further improvement of the new brake disc.

To obtain a clear heat transfer distribution contrast to the fuzzy distribution shown in Fig. 8(a) caused by the low frame rate of the infrared camera, a distinct experimental method is introduced in this study. The brake disc is first heated up at $N = 800$ rpm. Once the heat transfer becomes steady-state, temperature field on the inboard copper foil surface is measured as reference, from which the area-averaged temperature ($T_{w,\ mr}$) is calculated. Afterwards, the heating elements are turned off, followed by deceleration of the brake disc to 0 rpm in approximately 9 s. The surface temperature field is immediately measured, from which the area-averaged temperature ($T_{w,\ ms}$) is calculated. Subsequently, the temperature field obtained from the stationary brake disc is scaled up by a constant factor of $T_{w,\ mr}/T_{w,\ ms}$ as the final result. Due to thermal inertia of the brake disc, surface temperature gradient cannot be totally balanced in a short period, enabling a clear heat transfer distribution obtainable.

Fig. 10 presents the measured local heat transfer characteristics for both brake discs where the local effective Nusselt number (Nu_{Ro}) is calculated from Eq. (4). Again, the lower half distribution is a central symmetry of the upper half relative to the z-axis. For the radial vane brake disc, discontinuous vane material distribution and flow separation near the suction sides of the vanes [14,34] have been reported to cause highly non-uniform heat transfer on ventilated channel walls [34]. However, the local effective heat transfer obtained on the inboard copper foil surface is approximately isotropic along the circumferential direction, as indicated by the approximately concentric contour lines shown in Fig. 10(a). Thermal spreading in the inboard disc is responsible for such a phenomenon. For the X-type lattice cored brake disc, highly anisotropic heat transfer distribution is observed in Fig. 10(b). Regions nearby the most blocked and open orientations (i.e., OA and OB) of the lattice core show the lowest and highest Nusselt numbers, respectively, and smooth transition exists between these regions. Overall, the X-type lattice cored brake disc exhibits higher heat transfer, except the two hot spots which skew towards the counter-rotating direction from $\theta = 0°$ and 180°, respectively.

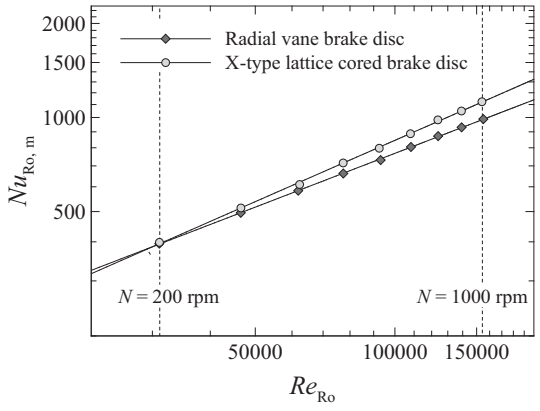

Fig. 9. Comparison of steady-state cooling performances of the brake discs at various rotating speed.

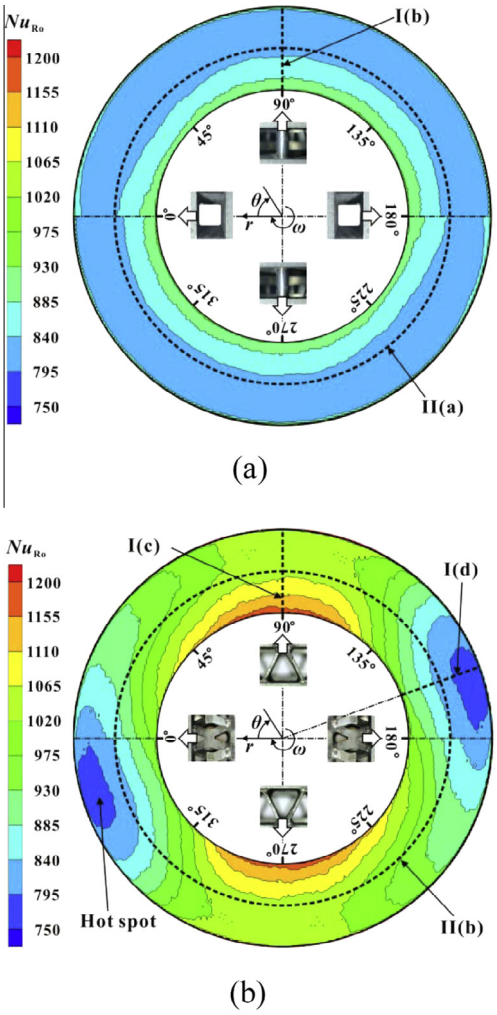

Fig. 10. Local heat transfer characteristics on inboard copper foil surface of brake disc at $N = 800$ rpm: (a) radial vane brake disc; (b) X-type lattice cored brake disc.

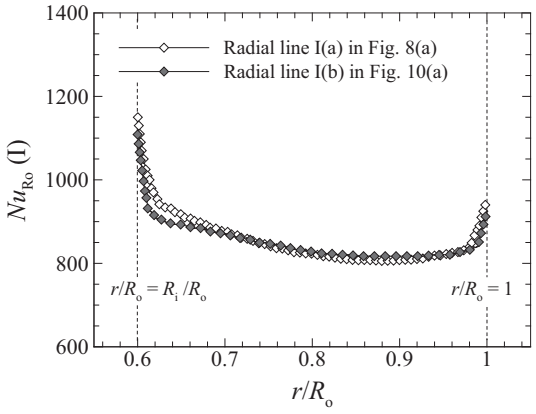

Fig. 11. Comparison of Nusselt number distributions along radial lines I(a) in Fig. 8(a) and I(b) in Fig. 10(a) for validation of experimental method.

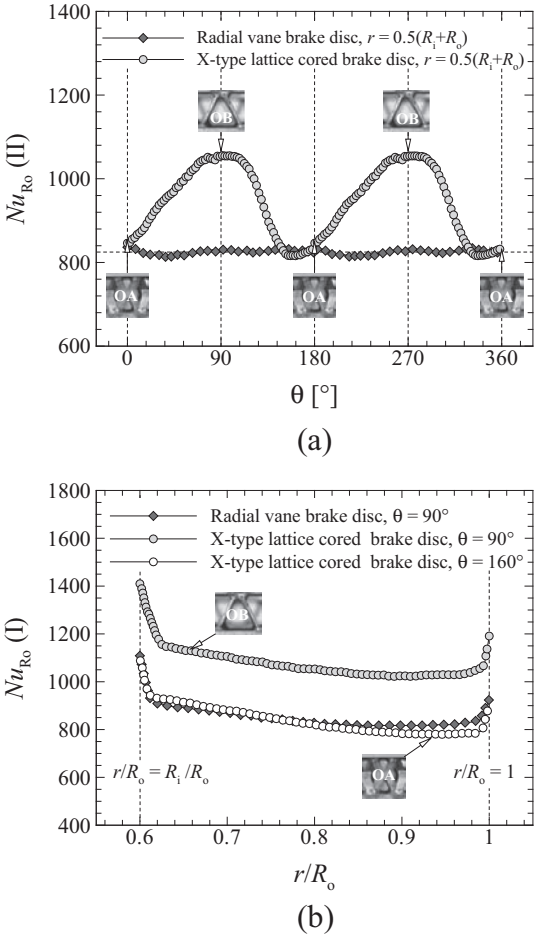

Fig. 12. Extracted profiles of Nusselt number along (a) circumferential lines II (a, b) and (b) radial lines I(b–d) depicted in Fig. 10.

The circumferentially isotropic heat transfer for the radial vane brake disc makes it feasible to validate the experimental method introduced in this section by comparing the estimated Nusselt number distribution along radial line I(b) in Fig. 10(a) with the accurate distribution along radial line I(a) in Fig. 8(a). Good agreement between these two profiles as revealed by Fig. 11 validates the present experimental method.

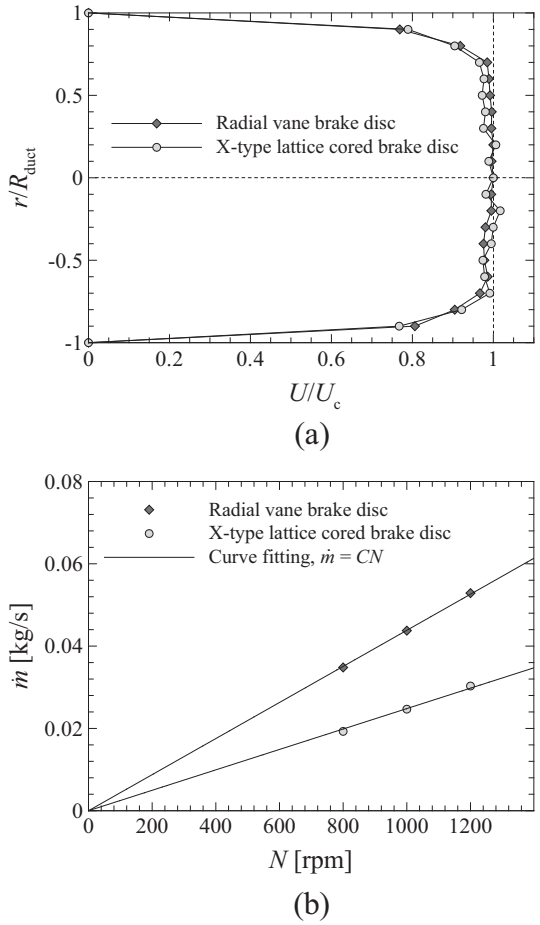

Fig. 13. Comparison of brake disc pumping capacity: (a) representative non-dimensional velocity profile measured in circular intake duct of Fig. 5(b); (b) pumping capacity plotted as a function of rotating speed.

For quantitative comparison, representative profiles of the Nusselt number extracted from Fig. 10 are plotted in Fig. 12. Fig. 12(a) presents the circumferential profiles at $r = 0.5(R_i + R_o)$. The radial vane brake disc has an approximately constant Nusselt number comparable to the lowest Nusselt number (at $\theta = 160°$ and 320°) for the X-type lattice cored brake disc. However, the new brake disc substantially outperforms the reference brake disc at $\theta = 90°$ and 270°, providing 27% more heat removal. The radial profiles displayed in Fig. 12(b) indicate comparable Nusselt numbers at $\theta = 160°$ for both brake discs. At $\theta = 90°$, however, the X-type lattice cored brake disc again provides up to 30% higher heat transfer than the radial vane brake disc.

3.3. Heat transfer enhancement by the lattice core

In view of the results shown in Figs. 8–12, it is of interest to understand: (1) why overall heat transfer enhancement can be achieved by the new brake disc in comparison with the reference one; (2) how the X-type lattice core induces circumferentially anisotropic heat transfer. To this end, a series of experiments are conducted.

First, mass flow rate of cooling flow sucked into the ventilated channel is measured to characterize the pumping capacity of both the new and reference brake discs. Fig. 13(a) shows representative profiles of axial velocity component (U) normalized by centerline velocity (U_c) in the circular intake duct (see Fig. 5(b)). It is seen that

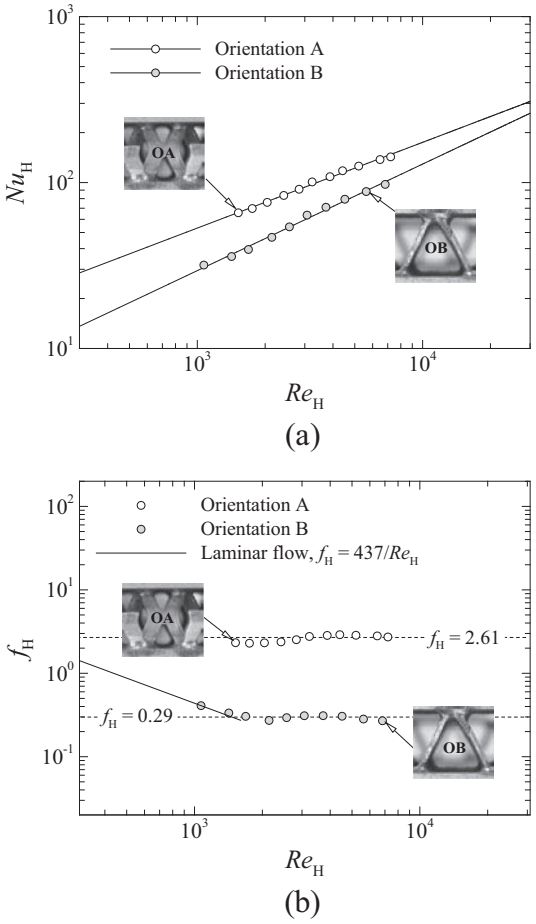

Fig. 14. Comparison of (a) overall heat transfer and (b) pressure drop in two orientations (i.e., OA and OB) of X-type lattice subjected to forced convection.

the flow is developing and symmetric with respect to the duct axis (z-axis). The mass flow rate of cooling flow is then calculated by integrating the velocity profile and correlated as a function of rotating speed (N), as:

$$\dot{m} = CN \tag{12}$$

where $C = 4.385 \times 10^{-5}$ and 2.482×10^{-5} for radial vane and X-type lattice cored brake discs, respectively. Eq. (12) indicates linear increase of mass flow rate with rotating speed for both brake discs, which is consistent with previous studies [14,17,25–27].

It may be concluded from Fig. 13(b) that the X-type lattice cored brake disc has 43% less pumping capacity than the radial vane brake disc. However, the X-type lattice core has 1.1 times more surface area density than the radial vane core. Consequently, it may be inferred that intensified flow mixing by the three-dimensional network of thin solid ligaments in an enlarged surface area is responsible for the superior overall cooling performance of the new brake disc (see Figs. 8 and 9).

To understand the anisotropic heat transfer pattern of the X-type lattice cored brake disc (see Fig. 10), forced convective pressure drop and heat transfer in the most blocked and open orientations (i.e., OA and OB) of the X-type lattice are characterized in a stationary wind tunnel. The results are presented in Fig. 14.

Overall heat transfer of the X-type lattice sandwich panels are compared in Fig. 14(a). The Nusselt number is correlated as a function of Reynolds number as:

$$Nu_H = CRe_H^n \tag{13}$$

where $C = 1.4965$ and $n = 0.5168$ for OA; $C = 0.3491$ and $n = 0.6421$ for OB. For a given Reynolds number or mass flow rate, it is evident that OA outperforms OB, providing approximately 40–80% more heat removal in the present Reynolds number range of $1100 < Re_H < 7200$. For the X-type lattice cored brake disc, on the contrary, region nearby OB provides up to 30% more heat removal than that nearby OA as shown in Fig. 12. Thus it can be inferred that OB sucks more coolant into the ventilated channel than OA for a given rotating speed.

The pressure drop characteristics of both orientations are compared in Fig. 14(b). For OB, the flow appears to be laminar when $Re_H < 1500$; whereas transition and turbulent flow occurs when $Re_H > 1500$. For OA, the friction factor is approximately independent of Reynolds number, exhibiting a constant value of 2.61. Overall, OB causes 8 times less pressure drop than OA. Such substantially lower pressure drop is believed to be the dominant reason for the superior pumping capacity nearby OB relative to OA in the X-type lattice cored brake disc.

4. Conclusions

To further improve the cooling performance of disc brake systems, the present study proposes a new concept of bidirectional ventilated brake disc incorporating a high porosity X-type lattice core. A series of transient and steady-state experiments in both rotating and stationary environments are conducted to characterize its thermo-fluidic behaviors, with direct comparison to a prevalent radial vane brake disc. Conclusions drawn in this study are summarized as follows.

(1) During short time braking, both brake discs exhibit comparable cooling performance. During long time braking, however, the X-type lattice cored brake disc provides up to 14% more heat removal than the radial vane brake disc.
(2) Anisotropic morphology of the X-type lattice core induces circumferentially anisotropic heat transfer pattern in the disc. Relative to the radial vane brake disc, regions nearby the most open orientation of the lattice core provides 30% more heat removal, whereas regions nearby the most blocked orientation of the lattice core provide comparable heat transfer.
(3) Although the new brake disc exhibits 43% less pumping capacity, more complex flow mixing and 1.1 times more heat transfer area induced by the lattice core are responsible for its superior cooling performance.
(4) For a given cooling rate, the most open orientation of the lattice core provides up to 80% less heat transfer than the most blocked orientation. However, higher pumping capacity due to 8 times less pressure drop enables higher transfer in regions nearby the most open orientation of the new brake disc for a given rotating speed.

Conflict of interest

None declared.

Acknowledgments

This research was supported by the National Basic Research Program of China (Grant No. 2011CB610305) and the Major International Joint Research Program of China (Grant No. 11120101002). The authors would like to thank Prof. T. Kim from University of the Witwatersrand for constructive discussion with him.

References

[1] T.H. Thomas, Disc brakes "two years after", SAE Paper No. 670197.
[2] R. Limpert, Brake Design and Safety, second ed., Society of Automobile Engineers Inc., Warrendale, USA, 1999.
[3] E. Palmer, R. Mishra, J. Fieldhouse, J. Layfield, Analysis of air flow and heat dissipation from a high performance GT car front brake, SAE Paper No. 2008-01-0820.
[4] A. Belhocine, M. Bouchetara, Thermal analysis of a solid brake disc, Appl. Therm. Eng. 32 (2012) 59–67.
[5] M. Pevec, I. Potrc, G. Bombek, D. Vranesevic, Prediction of the cooling factors of a vehicle brake disc and its influence on the results of a thermal numerical simulation, Int. J. Automobile Technol. 13 (5) (2012) 725–733.
[6] K. Lee, Numerical prediction of brake fluid temperature rise during braking and heat soaking, SAE Paper No. 1999–01-0483.
[7] I. Ahmed, P.S. Leung, P.K., Datta, Experimental investigations of disc brake friction, SAE Paper No. 2000-01-2778.
[8] M.H. Cho, S.J. Kim, R.H. Basch, J.W. Fash, H. Jang, Tribological study of gray cast iron with automotive brake linings: the effect of rotor microstructure, Tribol. Int. 36 (7) (2003) 537–545.
[9] J.E. Hunter, S.S. Cartier, D.J. Temple, R.C. Mason, Brake fluid vaporization as a contribution factor in motor vehicle collisions, SAE Paper No. 980371.
[10] S. Anoop, S. Natarajan, S.P. Kumaresh Babu, Analysis of factors influencing dry sliding wear behaviour of Al/SiC_p-brake pad tribosystem, Mater. Des. 30 (9) (2009) 3831–3838.
[11] T.J. Mackin, S.C. Noe, K.J. Ball, B.C. Bedell, D.P. Bim-Merle, M.C. Bingaman, D.M. Bomleny, G.J. Chemlir, D.B. Clayton, H.A. Evans, R. Gau, J.L. Hart, J.S. Karney, B.P. Kiple, R.C. Kaluga, P. Kung, A.K. Law, D. Lim, R.C. Merema, B.M. Miller, T.R. Miller, T.J. Nielson, T.M. O'Shea, M.T. Olson, H.A. Padilla, B.W. Penner, C. Penny, R.P. Peterson, V.C. Polidoro, A. Raghu, B.R. Resor, B.J. Robinson, D. Schambach, B.D. Snyder, E. Tom, R.R. Tschantz, B.M. Walker, K.E. Wasielewski, T.R. Webb, S.A. Wise, R.S. Yang, R.S. Zimmerman, Thermal cracking in disc brakes, Eng. Failure Anal. 9 (1) (2002) 63–76.
[12] C.H. Gao, J.M. Huang, X.Z. Lin, X.S. Tang, Stress analysis of thermal fatigue fracture of brake disks based on thermomechanical coupling, ASME J. Tribol. 129 (3) (2007) 536–543.
[13] D. Phan, D. Kondyles, Rotor design and analysis: a technique using computational fluid dynamics (CFD) and heat transfer analysis, SAE Paper No. 2003-01-3303.
[14] D.A. Johnson, B.A. Sperandei, R. Gilbert, Analysis of the flow through a vented automotive brake rotor, ASME J. Fluids Eng. 125 (6) (2003) 979–986.
[15] A. Belhocine, M. Bouchetara, Thermal behavior of full and ventilated disc brakes of vehicles, J. Mech. Sci. Technol. 26 (11) (2012) 3643–3652.
[16] T.C. Chatterley, M.P. Macnaughtan, Cast iron brake discs – current position, performance and future trends in Europe, SAE Paper No. 1999-01-0141.
[17] L. Wallis, E. Leonardi, B. Milton, P. Joseph, Air flow and heat transfer in ventilated disc brake rotors with diamond and tear-drop pillars, Numer. Heat Transfer A Appl. 41 (6–7) (2002) 643–655.
[18] S.M. Reddy, J.M. Mallikarjuna, V. Ganesan, Flow and heat transfer analysis of a ventilated disc brake rotor using CFD, SAE Paper No. 2008-01-0822.
[19] L. Wallis, a comparison of bi-directional disc brake rotor passage designs (Ph.D. thesis), The university of New South Wales, Sydney, Australia, 2003.
[20] G. Barigozzi, G.E. Cossali, A. Perdichizzi, S. Lorenzo, P. Pacchiana, Experimental investigation of the aero-thermal characteristics at the exit of an automotive vented brake disc, SAE Paper No. 2003-01-3338.
[21] G. Barigozzi, A. Perdichizzi, M. Donati, Combined experimental and CFD investigation of brake discs aero-thermal performances, SAE Int J. Passeng. Cars Mech. Syst. 1 (1) (2009) 1194–1201.
[22] E. Palmer, R. Mishra, J. Fieldhouse, A computational fluid dynamic analysis on the effect of front row pin geometry on the aerothermodynamic properties of a pin-vented brake disc, IMechE J. Automobile Eng. 222 (7) (2008) 1231–1245.
[23] E. Palmer, R. Mishra, J. Fieldhouse, An optimization study of a multiple-row pin-vented brake disc to promote brake cooling using computational fluid dynamics, IMechE J. Automobile Eng. 223 (7) (2009) 865–875.
[24] R. Limpert, The thermal performance of automotive disc brakes, SAE Paper No. 750873.
[25] R. Limpert, Cooling analysis of disc brake rotors, SAE Paper No. 751014.
[26] A.E. Sisson, Thermal analysis of vented brake rotors, SAE Paper No. 780352.
[27] M.D. Hudson, R.L. Ruhl, Ventilated brake rotor air flow investigation, SAE Paper No. 971033.
[28] A. Stephens, S. Watkins, C. Dixon, Aerodynamic testing of a ventilated disc brake, SAE Paper No. 2003-01-0932.
[29] G. Barigozzi, A. Perdichizzi, P. Pacchiana, R. Goller, Aero-thermal characteristics of an automotive CCM vented brake disc, SAE Paper No. 2005-01-3930.
[30] P. Hwang, X. Wu, Y.B. Jeon, Repeated brake temperature analysis of ventilated braked disc on the downhill road, SAE Paper No. 2008-01-2571.
[31] A.D. McPhee, D.A. Johnson, Experimental heat transfer and flow analysis of a vented brake rotor, Int. J. Therm. Sci. 47 (4) (2008) 458–467.
[32] M. Kubota, T. Hamabe, Y. Nakazono, M. Fukuda, K. Doi, Development of a lightweight brake disc rotor: a design approach for achieving an optimum thermal, vibration and weight balance, JSAE Rev. 21 (3) (2000) 349–355.
[33] S.B. Park, K.S. Lee, D.H. Lee, An investigation of local heat transfer characteristics in a ventilated disc brake with helically fluted surfaces, J. Mech. Sci. Technol. 21 (12) (2007) 2178–2187.
[34] C.H. Galindo-Lopez, M. Tirovic, Understanding and improving the convective cooling of brake discs with radial vanes, IMechE J. Automobile Eng. 222 (7) (2008) 1211–1229.
[35] A. Nejat, M. Aslani, E. Mirzakhalili, R. Najian Asl, Heat transfer enhancement in ventilated brake disk using double airfoil vanes, ASME J. Therm. Sci. Eng. Appl. 3 (4) (2011) 045001-1–045001-10.
[36] C. Qian, Aerodynamic shape optimization using CFD parametric model with brake cooling application, SAE Paper No. 2002-01-0599.
[37] A.R. Daudi, 72 Curved fins and air director idea increases airflow through brake rotors, SAE Paper No. 1999-01-0140.
[38] A.R. Daudi, 72 Curved fin rotor design reduces maximum rotor temperature, SAE Paper No. 1999-01-3395.
[39] K.M. Munisamy, N.H. Shuaib, M.Z. Yusoff, S.K. Thangaraju, Heat transfer enhancement on ventilated brake disk with blade inclination angle variation, Int. J. Automotive Technol. 14 (4) (2013) 569–577.
[40] D. Parish, D.G. MacManus, Aerodynamic investigations of ventilated brake discs, IMechE J. Automobile Eng. 219 (2005) 471–486.
[41] H.N.G. Wadley, Multifunctional periodic cellular metals, Philos. Trans. R. Soc. A: Math., Phys. Eng. Sci. 364 (1838) (2006) 31–68.
[42] T. Kim, C.Y. Zhao, T.J. Lu, H.P. Hodson, Convective heat dissipation with lattice-frame materials, Mech. Mater. 36 (8) (2004) 767–780.
[43] J.H. Joo, K.J. Kang, T. Kim, T.J. Lu, Forced convective heat transfer in all metallic wire-woven bulk Kagome sandwich panels, Int. J. Heat Mass Transfer 54 (25) (2011) 5658–5662.
[44] S.S. Feng, M.Z. Li, J.H. Joo, K.J. Kang, T. Kim, T.J. Lu, Thermomechanical properties of brazed wire-woven bulk Kagome cellular metals for multifunctional applications, J. Thermophys. Heat Transfer 26 (1) (2012) 66–74.
[45] Y.-H. Lee, B.-K. Lee, I. Jeon, K.-J. Kang, Wire-woven bulk Kagome truss cores, Acta Mater. 55 (18) (2007) 6084–6094.
[46] V.S. Deshpande, N.A. Fleck, M.F. Ashby, Effective properties of the octet-truss lattice material, J. Mech. Phys. Solids 49 (8) (2001) 1747–1769.
[47] D.T. Queheillalt, H.N.G. Wadley, Cellular metal lattices with hollow trusses, Acta Mater. 53 (2) (2005) 303–313.
[48] H.N.G. Wadley, N.A. Fleck, A.G. Evans, Fabrication and structural performance of periodic cellular metal sandwich structures, Comput. Sci. Technol. 63 (16) (2003) 2331–2343.
[49] G.W. Kooistra, H.N.G. Wadley, Lattice truss structures from expanded metal sheet, Mater. Des. 28 (2) (2007) 507–514.
[50] Q.C. Zhang, Y.J. Han, C.Q. Chen, T.J. Lu, Ultralight X-type lattice sandwich structure (I): concept, fabrication and experimental characterization, Sci. China Ser. E: Technol. Sci. 52 (8) (2009) 2147–2154.
[51] Q.C. Zhang, A.P. Chen, C.Q. Chen, T.J. Lu, Ultralight X-type lattice sandwich structure (II): micromechanics modeling and finite element analysis, Sci. China Ser. E: Technol. Sci. 52 (9) (2009) 2670–2680.
[52] T. Wen, J. Tian, T.J. Lu, D.T. Queheillalt, H.N.G. Wadley, Forced convection in metallic honeycomb structures, Int. J. Heat Mass Transfer 49 (19) (2006) 3313–3324.
[53] H.B. Yan, Q.C. Zhang, T.J. Lu, T. Kim, A lightweight X-type metallic lattice for single-phase forced convection, Int. J. Heat Mass Transfer, submitted for publication (manuscript No. HMT-D-14-00833).
[54] H.W. Coleman, W.G. Steele, Experimentation, Validation, and Uncertainty Analysis for Engineers, third ed., John Wiley & Sons Inc., Hoboken, New Jersey, 2009.